Communication

Synthesis of (Cu,Mn,Co)$_3$O$_4$ Spinel: Effects of Citrate-to-Nitrate Ratio on Its Homogeneity and Electrical Properties

Joelle C. W. Mah [1], Isyraf Aznam [1,2], Andanastuti Muchtar [1,3,*], Mahendra Rao Somalu [1] and Jarot Raharjo [4]

1. Fuel Cell Institute, Universiti Kebangsaan Malaysia, Bangi 43600, Selangor Darul Ehsan, Malaysia
2. Material Sciences Division, Gaia Science (M) Sdn Bhd, Puchong 47100, Selangor Darul Ehsan, Malaysia
3. Department of Mechanical and Manufacturing Engineering, Faculty of Engineering and Built Environment, Universiti Kebangsaan Malaysia, Bangi 43600, Selangor Darul Ehsan, Malaysia
4. Research Center for Advanced Materials, National Research and Innovation Agency, Puspiptek, South Tangerang 15314, Banten, Indonesia
* Correspondence: muchtar@ukm.edu.my

Abstract: The (Cu,Mn,Co)$_3$O$_4$ (CMC) spinel layer is useful in inhibiting Cr vaporization that deteriorates the solid oxide fuel cell performance. The effectiveness of the spinel layer in suppressing volatile Cr species from the metallic interconnects is strongly dependent on layer density, which is influenced by particle size distributions and agglomerations of the spinel powders. Considering that the material properties were influenced by the synthesizing conditions, this study elucidated the influences of citric acid (fuel) on the structure, morphology, and electrical properties of sol–gel derived CMC spinel powders. Dual-phase CMC spinel powders, consisting of cubic CuMnCoO and tetragonal Mn$_2$CoO$_4$, were successfully synthesized at citrate-to-nitrate (CA/MN) ratios of 0.8, 1.0, and 1.2. An undesired CuCo$_2$O$_4$ phase was observed in spinel powders synthesized at a low CA/MN ratio of 0.5. The CA/MN ratio has influenced not only the phase formation of CMC spinel, but also the particle size distributions. The CA/MN ratio of 1.0 yielded the finest CMC spinel with the least agglomerates, which then produced the highest electrical conductivity of 116 Scm^{-1}. Therefore, the CA/MN ratio of 1.0 was recommended for the synthesis of CMC spinel, which can be used in fabricating the protective coating of solid oxide fuel cell interconnects.

Keywords: solid oxide fuel cells; spinels; sol–gel processes; agglomerations; electrical properties

1. Introduction

Progressive efforts in developing solid oxide fuel cells (SOFCs) that operate at a temperature ranging from 500 °C to 800 °C have facilitated the use of metallic interconnects as substitutes for conventional ceramic interconnects [1,2]. However, excessive Cr$_2$O$_3$-scale growth and Cr vaporization from metallic interconnects to the cathode/electrolyte interface causes severe cell degradation [3–5]. Research is trending toward the development of protective layers that improve the performance of SOFCs [6–9]. (Cu,Mn,Co)$_3$O$_4$ (CMC) spinel exhibits considerable potential as a barrier to suppress the outward diffusion of Cr from metallic interconnects [10]. The effectiveness of the spinel layer in suppressing inter-diffusion behavior is highly dependent on the layer density; in particular, the rate of Cr vaporization in a porous layer can be three times higher than the denser counterpart [11,12]. Given that the layer density of the deposited layer is influenced by the homogeneity of the spinel powders, particularly particle size distribution and the degree of agglomeration of the spinel powders [13,14], the determination of a suitable fuel-to-nitrate ratio that produces homogenous particle size distribution and a low degree of agglomeration is essential, before depositing the protective layer and assessing the inter-diffusion behavior.

Rapid development in sol–gel synthesis produced nanoceramics with enhanced microstructures and photocatalytic properties, which are crucial for energy conversion and

storage applications [15]. The Pechini sol–gel method chelates the metal cations with citric acid (CA) and poly-esterifies the chelated metal–citrate complexes with ethylene glycol (EG), forming a highly branched polymeric gel precursor with two or more metal cations dispersed homogeneously throughout the network, which is of particular interest [16,17]. In a typical Pechini sol–gel synthesis, a homogeneous precursor solution containing metal–citrate chelated complexes is prepared by mixing the metal nitrates solution with a CA, followed by subsequent heating to initiate poly-esterification between the metal–citrate complexes and EG, forming a polymeric metal/organic gel precursor. The organic matrix is then decomposed in the subsequent combustion to form the desired oxide powders. The crosslinking reaction that occurred during chelation and poly-esterification is presented in Figure 1. Pechini sol–gel synthesis is of particular interest because of its capability to form a highly branched polymeric gel precursor with two or more metal cations dispersed homogeneously throughout the network (Figure 2) [18].
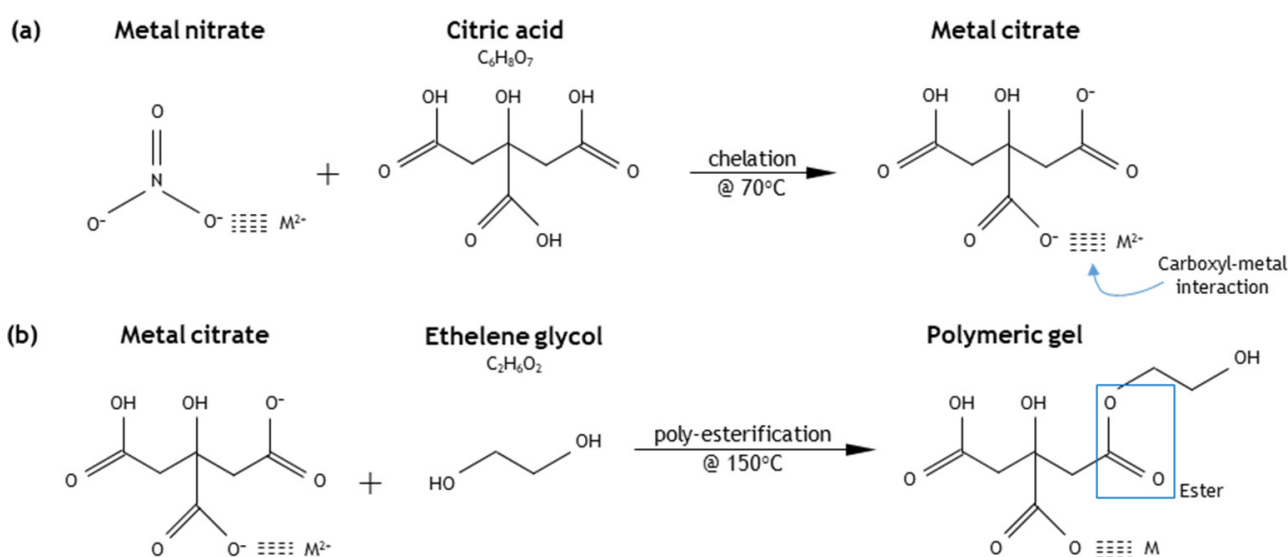
Figure 1. Schematic of the crosslinking reaction, which occurred during (**a**) chelation and (**b**) poly-esterification.
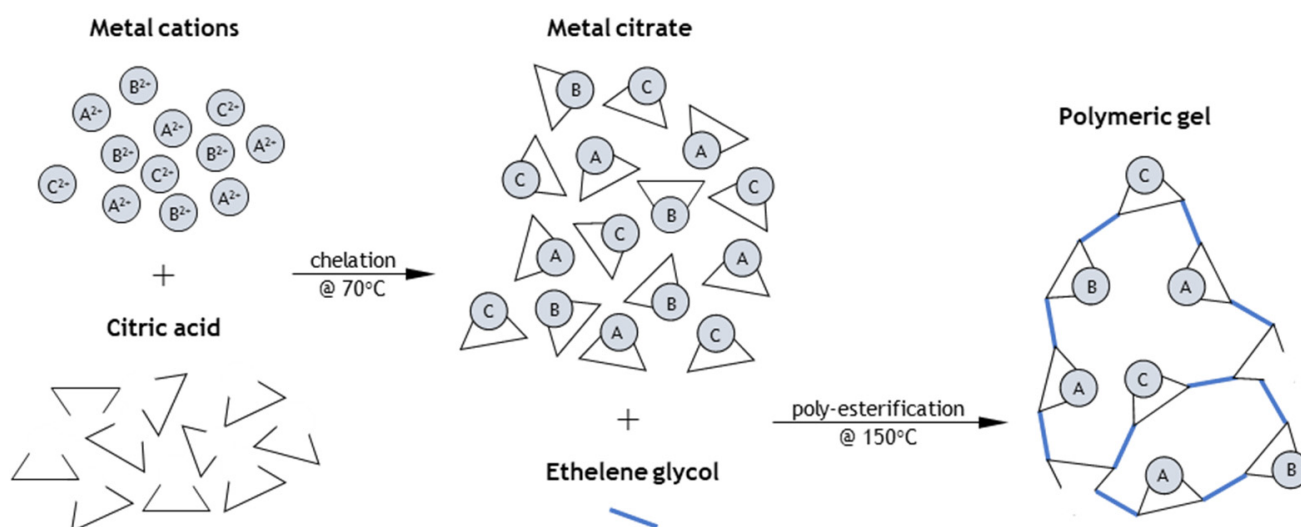
Figure 2. Schematic of the polymeric metal/organic gel precursor produced through the Pechini sol–gel method.

The $CoFe_2O_4$ spinel powders are synthesized via the sol–gel method using three different fuels, namely EG, glycine, and urea. Powders with small particle sizes (an average of 15 nm) were obtained when being synthesized using urea, whereas powders prepared through EG resulted in improved magnetic properties [19]. Increasing the citrate-to-nitrate (CA/MN) ratio above the stoichiometric molar ratio (0.78) in synthesizing $Ce_{0.9}Gd_{0.1}O_{1.95}$ results in a high combustion temperature with a substantial amount of residue ash and a large crystallite size with a high degree of agglomeration [20]. Moreover, the variation of CA/MN ratios improves the physicochemical properties and catalytic performance of $LaMnO_3$ perovskite. CA/MN ratios range between 1.1 and 1.5, yielding a high Mn/La surface atomic ratio, a high specific surface area, and a high Mn reducibility, which are influential factors in hydrocarbon oxidation reactions [21]. Although the effects of fuel type [22,23] and the fuel-to-nitrate ratio [21,24] on the formation and properties of nano-ceramic powders are widely studied, few reported on CMC spinel powders. The formation and the structural stability of the spinel oxide are not only influenced by the CA/MN ratios, but also by the decomposition behavior of the metal nitrates [25,26]. The thermal decomposition behavior of the CMC spinel powders and the effects of calcination temperatures on the properties of the CMC spinel powders was investigated and reported in our previous work [27]. The present work aims to study the effect of CA as a chelating agent in the synthesis of CMC spinel for protective coating application. In this work, changes in the phase structure, particle size distribution, and electrical properties of the sol–gel derived CMC spinel powders were investigated by manipulating the amount of CA that acts as a fuel/chelating agent.

2. Materials and Methods

The metal nitrates ($Mn(NO_3)_2 \cdot 4H_2O$, $Co(NO_3)_2 \cdot 6H_2O$, and $Cu(NO_3)_2 \cdot 3H_2O$; Merck) in a molar ratio of 1:1:1 were dissolved in deionized water to prepare an aqueous solution. CA ($C_6H_8O_7$; Merck) and EG ($C_2H_6O_2$; Merck) were added at 70 °C under continuous stirring conditions. The CA/MN ratio varied from 0.5 to 0.8, 1.0, and 1.2, whereas the EG-to-nitrate ratio was maintained at 1.5. The resulting gel-like precursor was dried at 200 °C and calcined at 800 °C [27].

An X-ray diffractometer (XRD; D8-Advance; Bruker) was used to determine the phase formation of the spinel powders synthesized at different CA/MN ratios. With reference to the XRD patterns, the degree of crystallinity and percentage of each constituent phase of the spinel powders were determined using semi-quantitative analysis, and the crystallite size was determined using Scherrer's equation. Once the diffraction peaks in the XRD pattern obtained are identified using the classic search/match procedures, the degree of crystallinity can be determined by measuring areas under the curve.

$$\%_{crystalinity} = \frac{Area\ of\ crystalline\ peaks}{Area\ of\ total\ scan} \times 100, \tag{1}$$

The percentage of each constituent phase can be semi-quantitatively determined by comparing the integrated intensity of the diffraction peaks to those in the pure phase using Klug's equation [28]:

$$\%_{\alpha\ phase} = \frac{(I_\alpha{}^{meaasure}/I_\alpha{}^{pure})A_\beta}{A_\alpha - (I_\alpha{}^{measure}/I_\alpha{}^{pure})(A_\alpha - A_\beta)}, \tag{2}$$

where $I_\alpha{}^{measure}$ and $I_\alpha{}^{pure}$ are the intensity of α phase measured in the XRD results and pure material, respectively. A_α and A_β are the mass absorption coefficients of the α and β phase, respectively.

The morphology of the spinel powders synthesized at different CA/MN ratios was investigated by field emission scanning electron microscopy (FESEM; Supra55VP; Carl Zeiss, Germany). Different particle size analysis techniques detected size through their physical principle. In this work, the particle size distributions of the synthesized spinel

powders were measured through dynamic light scattering (DLS) analysis. The spinel powders were dispersed in deionized water at 0.01 g/L and ultrasonicated prior to collecting the DLS data. The synthesized powders were uniaxially pressed to form a circular pellet using a 25 mm diameter mold. After that, the green pellet was sintered in air at 1200 °C for 4 h using a muffle furnace (Berkeley Scientific BSK-1700X-S, Berkeley, CA, USA). The sintered pellet was then used to measure DC conductivity (σ) using a four-point Van der Pauw method [29] from 500 °C to 800 °C in air. Pt wires were used as contact points in the measurement system.

3. Results and Discussion

3.1. CMC Spinel Powders

A dual-phase structure, consisting of cubic $CuMnCoO_4$ (ICDD card n.: 47-0324) and tetragonal Mn_2CoO_4 (ICDD card n.: 77-0471), was formed at the calcination temperature of 800 °C at the CA/MN ratio of 0.8, 1.0 and 1.2 (Table 1). The diffraction peaks of cubic $CuMnCoO_4$ (ICDD card n.: 47-0324) were slightly shifted to a higher theta angle, resulting in a cubic $CuCo_2O_4$ (ICDD card n.: 73-2752) structure when the CA/MN ratio was lowered to 0.5 (Figure 3). The formation of the $CuCo_2O_4$ phase and the low degree of crystallinity (59.0%) revealed the incomplete chelation of metal cations and the segregation of cations. This phenomenon was primarily caused by insufficient combustion for oxide synthesis [30]. The CA/MN ratio of 0.5, which yielded the lowest amount of cubic phase, was not recommended because the cubic phase should present superior electrical properties than those of the tetragonal phase [31].

Table 1. Degree of crystallinity, the percentage of each constituent phase, and the crystallite size of the spinel powders synthesized at different CA/MN ratios.

CA/MN	0.5	0.8	1.0	1.2
Crystallinity	59.0%	90.3%	88.5%	77.8%
$CuCo_2O_4$ Cubic (a = 0.8140 nm)	22.6%	-	-	-
Mn_2CoO_4 Tetragonal (a = 0.8090 nm, c = 0.9270 nm)	77.4%	41.8%	44.3%	45.7%
$CuMnCoO_4$ Cubic (a = 0.8189 nm)	-	58.2%	55.7%	54.3%
Crystallite size	21 nm	19 nm	21 nm	26 nm

A crystallite is defined as the smallest homogeneous crystallographic structure with a specific space orientation [32], that is, a perfect single crystal separated by the disorientation of its neighboring crystal. The crystallite size was determined by using Scherrer's equation:

$$D = k\lambda/\beta \cos\theta, \tag{3}$$

where D is the crystallite size; k is a dimensionless shape factor; λ is the wavelength of radiation; β is the full width at half of the maximum peak (FWHM) in radians and θ is the Bragg angle of the corresponding crystallographic plane. Referring to the maximum peak at 36.4°, an estimation value was computed and tabulated in Table 1. The finest crystallite size was yielded at a CA/MN of 0.8 but was insignificant.

All powders synthesized at different CA/MN ratios exhibited fine homogeneous spherical-like particles (Figure 4). Although the variations in CA/MN ratio exerted no influence on the shape of the particles, agglomerates were observed in those synthesized at the CA/MN ratio of 0.8 (Figure 4b) and 1.2 (Figure 4d). The particle size distributions of the spinel powders synthesized at the CA/MN ratios of 0.8, 1.0, and 1.2 were quantified using the DLS technique (Figure 5). In the DLS technique, various dimensions measured as the particles flew randomly through the light beam were averaged, thereby distributing sizes from the smallest to the largest dimensions. The size of the particles was represented

by the most frequently occurring diameter (maximum peak) in the particle size distributions, whereas the span of distributions indicated the degree of agglomeration. Although the CA/MN ratio of 0.5 yielded the finest particle size, this result was not acceptable because of the formation of the $CuCo_2O_4$ phase (Table 1). Spinel powders synthesized at the stoichiometric composition (1.0) exhibit better homogeneity and phase purity than those synthesized at a fuel-lean (0.8) and fuel-rich ratio (1.2). Given that optimal SOFC performances can be achieved at a low degree of agglomeration [33–35], the CA/MN ratio of 1.0 which yielded the highest homogeneity among the successfully synthesized spinel powders was recommended.
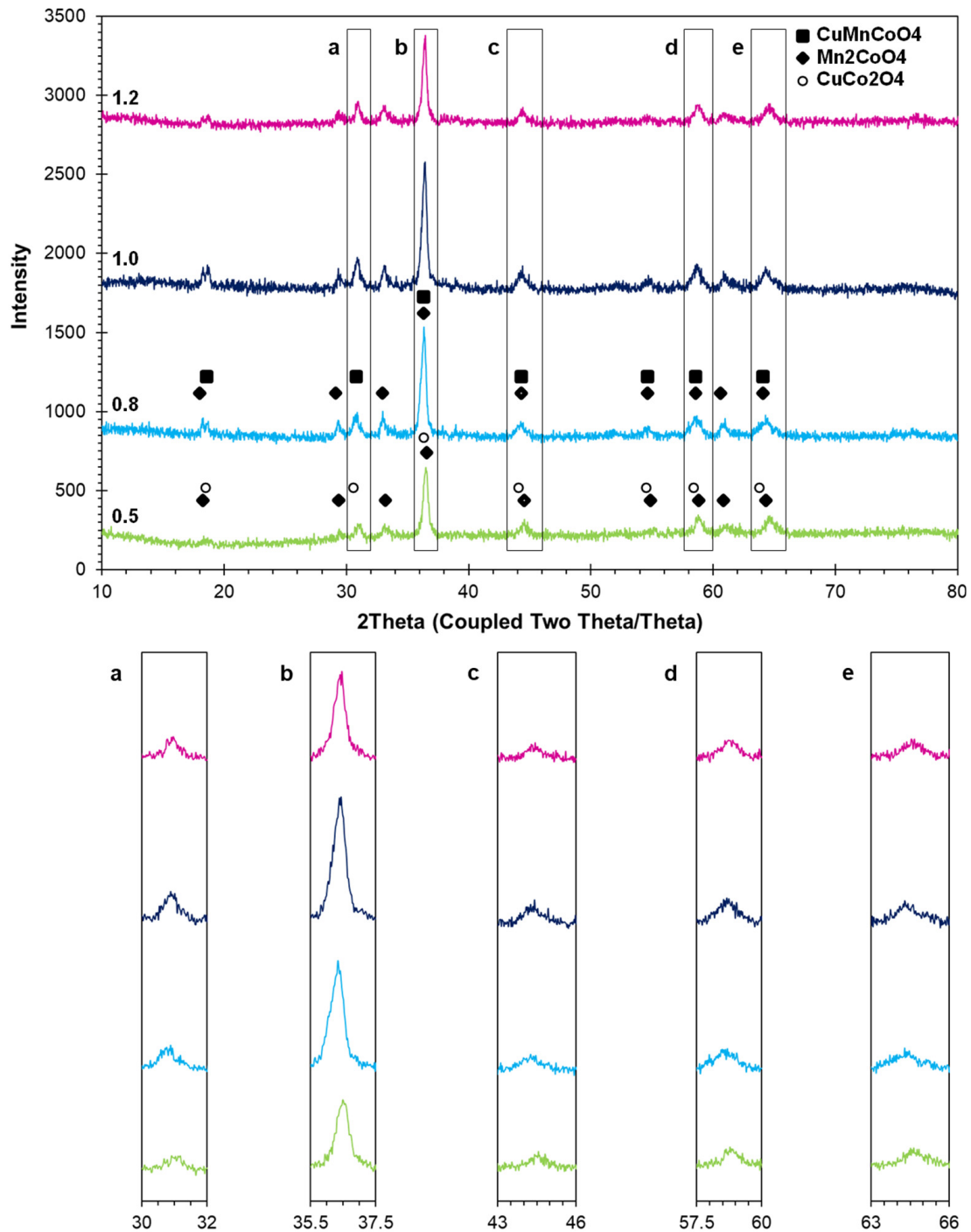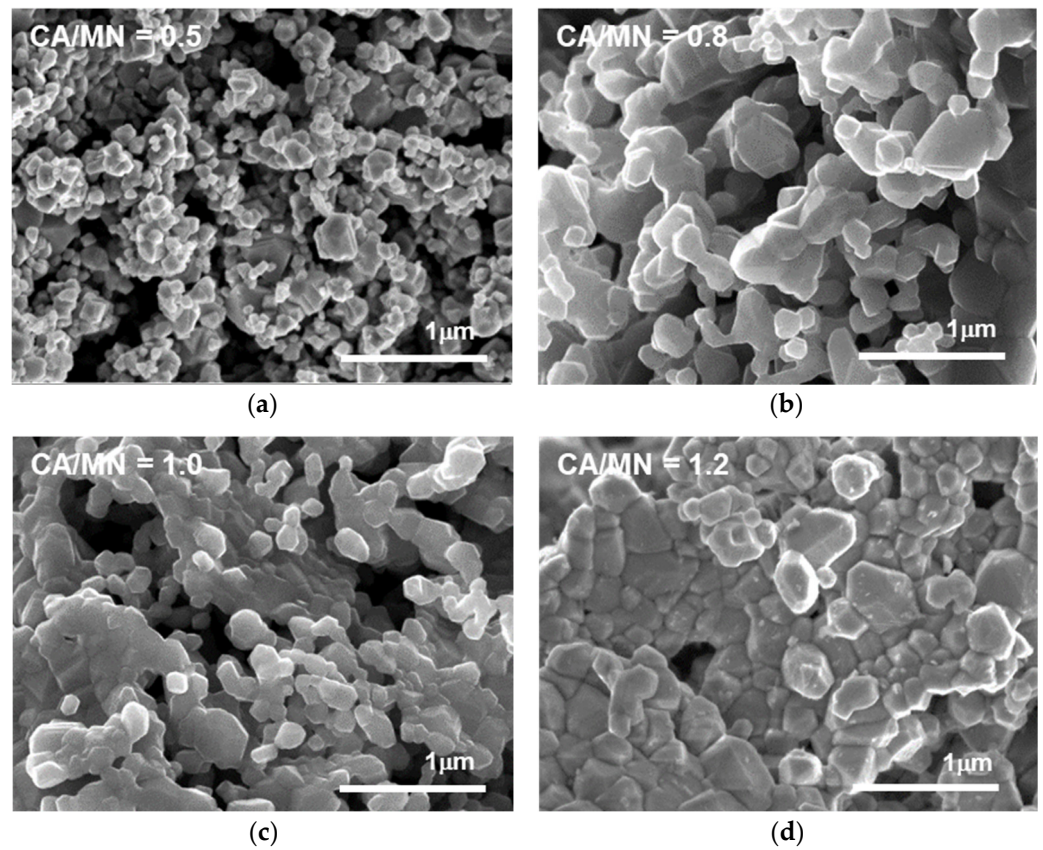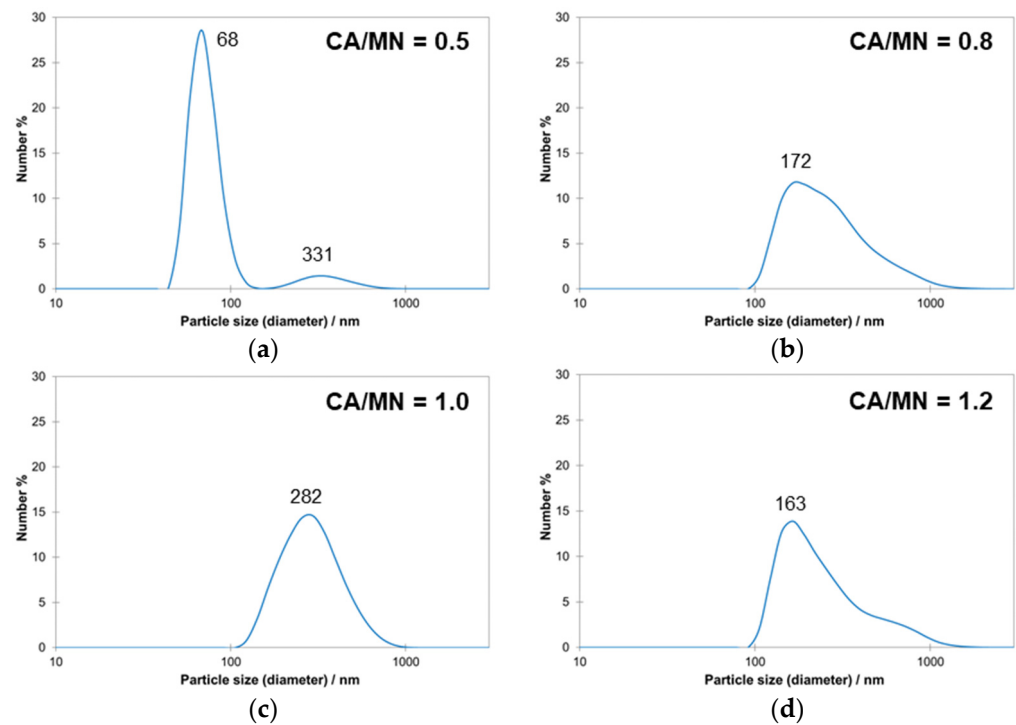

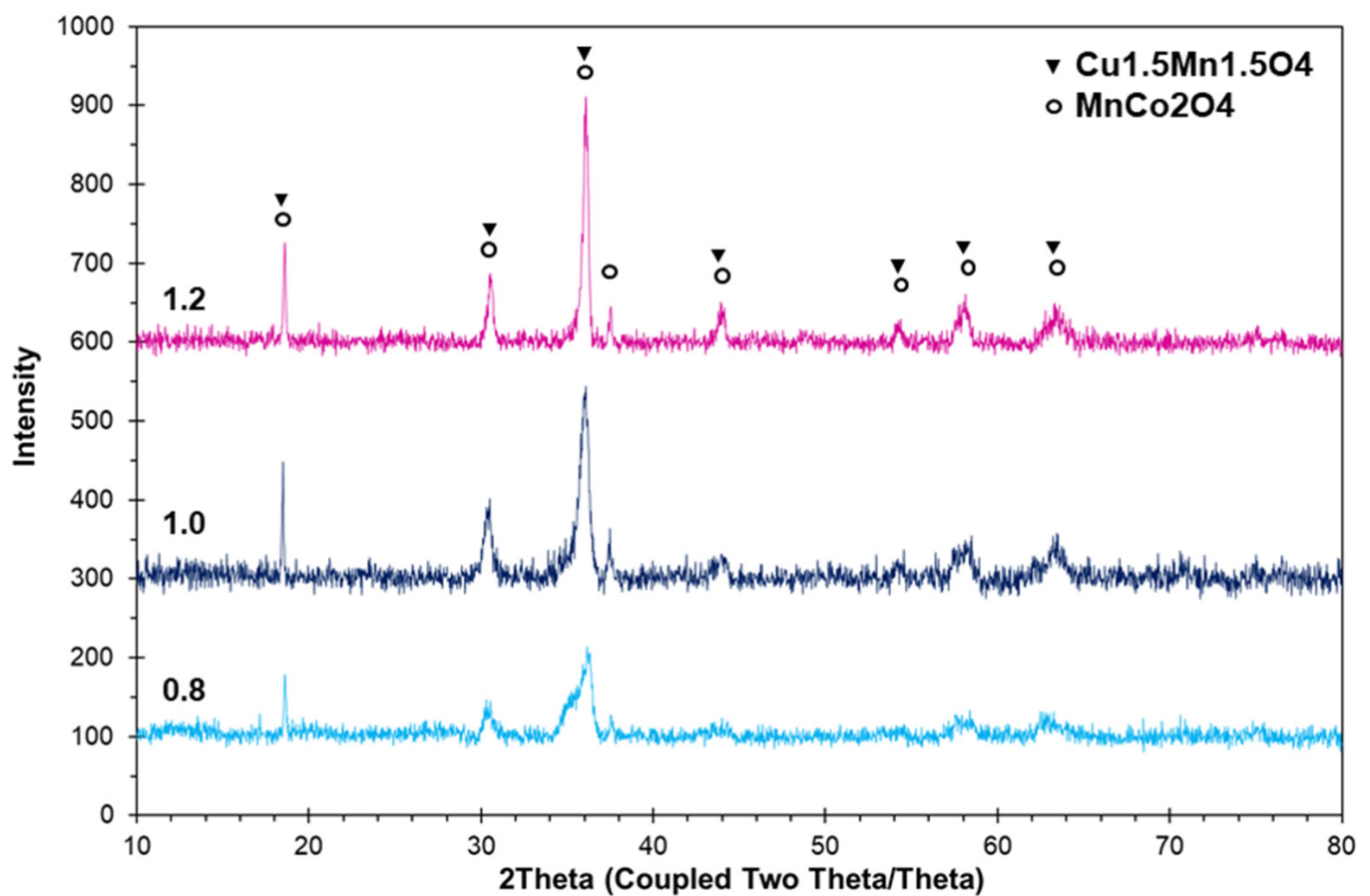**Figure 3.** X-ray diffraction patterns for the spinel powders synthesized at different CA/MN ratios.

Figure 4. Morphologies of spinel powders synthesized at CA/MN ratios of (**a**) 0.5, (**b**) 0.8, (**c**) 1.0, and (**d**) 1.2.

Figure 5. Particle size distributions of spinel powders synthesized at CA/MN ratios of (**a**) 0.5, (**b**) 0.8, (**c**) 1.0, and (**d**) 1.2.

3.2. CMC Spinel Sintered at 1200 °C

The CMC spinel synthesized at CA/MN ratios was pelletized and sintered at 1200 °C. All diffraction peaks in the XRD patterns in Figure 6 well match the cubic $MnCo_2O_4$ (ICDD card no. 23-1237) and the cubic $Cu_{1.5}Mn_{1.5}O_4$ (ICDD card no. 35-1171). The diffraction peaks of the tetragonal–cubic structure observed in the CMC spinel powders were slightly shifted to a lower theta, resulting in a cubic–cubic structure after sintering at 1200 °C. The disappearance of the tetragonal phase anticipates better electrical conduction, which is driven by a hopping mechanism of cations with different valence states between octahedral sites. The degree of crystallinity, percentage of each constituent phase computed through a semi-qualitative technique, and grain size of the pelletized CMC spinel sintered at 1200 °C are tabulated in Table 2. The highest degree of crystallinity (70.0%) was yielded at the CA/MN ratio of 1.0, followed by those synthesized at a fuel-lean (62.1%) and fuel-rich ratio (60.4%).

Figure 6. X-ray diffraction patterns for the pelletized CMC spinel sintered at 1200 °C.

Table 2. Degree of crystallinity, percentage of each constituent phase of and grain size of the pelletized CMC spinel sintered at 1200 °C.

CA/MN	0.8	1.0	1.2
Crystallinity	62.1%	70.0%	60.4%
$MnCo_2O_4$ Cubic (a = 0.8269 nm)	49.0%	46.4	46.1
$Cu_{1.5}Mn_{1.5}O_4$ Cubic (a = 0.8300 nm)	51%	53.6	53.9
Grain size	15.14 μm	15.85 μm	13.97 μm

Microstructures of the pelletized CMC spinel sintered at 1200 °C examined using FESEM are shown in Figure 7. Homogenous spinel powders synthesized at a CA/MN ratio of 1.0 resulted in a dense microstructure, whereas a porous microstructure was found in those agglomerated spinel powders synthesized at the CA/MN ratios of 0.8 and 1.2.
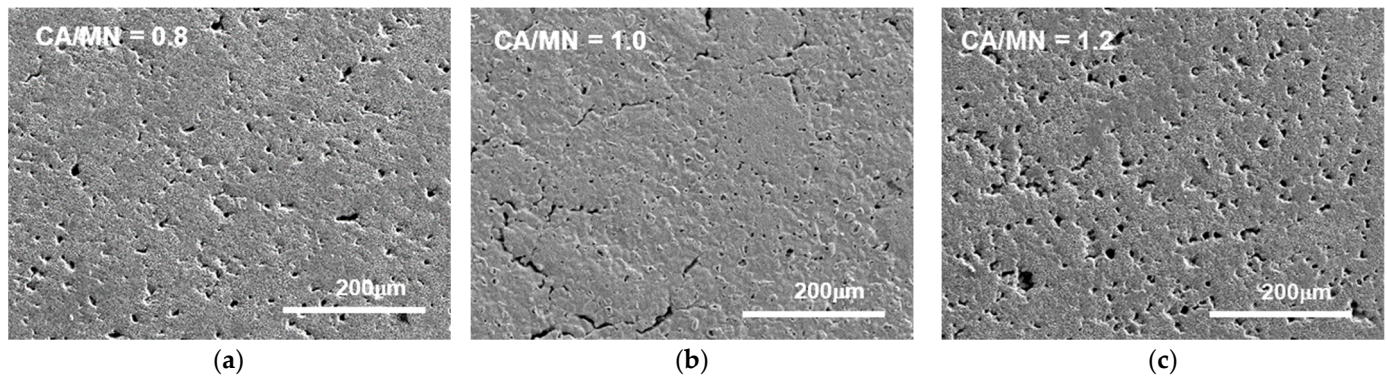
Figure 7. Microstructure of the pelletized CMC spinel sintered at 1200 °C using spinel powders synthesized at CA/MN ratios of (**a**) 0.8, (**b**) 1.0, and (**c**) 1.2.
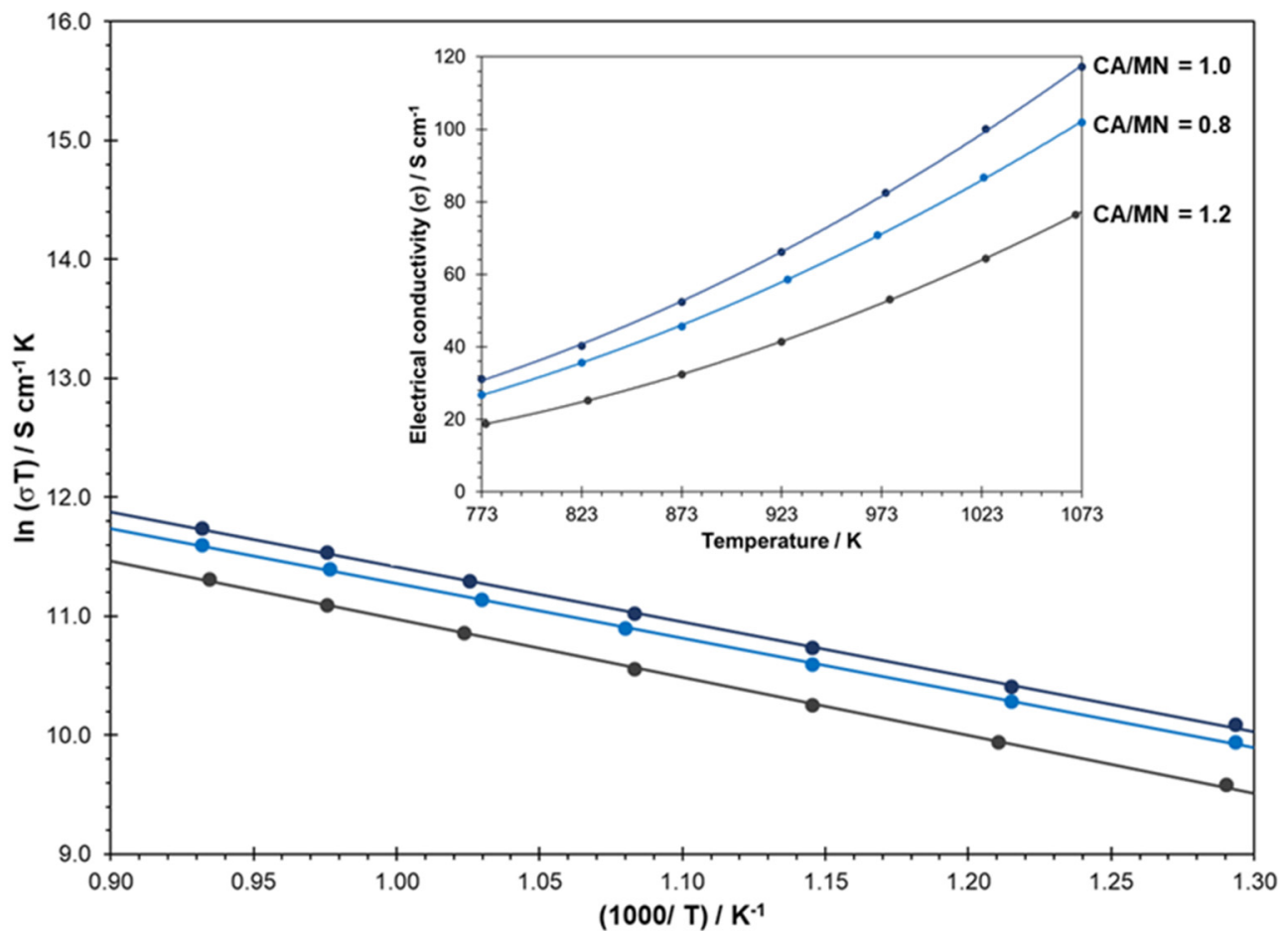
The DC electrical conductivity of a spinel, particularly that in manganese and cobalt families, is thermally activated through the small polarons hopping mechanism [36]. This hopping mechanism can be explained by the Arrhenius law in the natural logarithmic form [37]:

$$\ln \sigma T = \ln C - \frac{E_a}{kT}, \tag{4}$$

where σ is the specific conductivity (Scm^{-1}), T is the absolute temperature (K), C is a material constant containing the carrier concentration term (Scm^{-1} K), E_a is the activation energy for electrical conduction (eV), and k is the Boltzmann's constant (8.617×10^{-5} eV K^{-1}).

The synthesized powders were pelletized and sintered at 1200 °C prior to measuring the DC conductivity (σ) using a four-point Van der Pauw method from 500 °C to 800 °C. The linearity between ln (σT) and 1/T in the Arrhenius plot (Figure 8) was ascribed to the semiconductor behavior of the sol–gel derived CMC spinel. CMC spinel synthesized at the CA/MN ratio of 1.2 required a high activation energy of 0.4194 eV. The activation energies in the spinel powders synthesized at the CA/MN ratios of 0.8 (0.3974 eV) and 1.0 (0.3975 eV) were nearly constant. The electrical conductivity was correspondingly higher in powders with fine particle sizes and reduced agglomerates. The highest electrical conductivity of 116 Scm^{-1} was obtained from CMC spinel synthesized at the CA/MN ratio of 1.0, followed by 102 and 76 Scm^{-1} obtained from those synthesized at the CA/MN ratio of 0.8 and 1.2, respectively. These results are consistent with the measured activation energy. In short, spinel powders with the highest homogeneity produce a dense microstructure and good electrical properties, while porous microstructure and poor electrical properties were obtained in the agglomerated spinel powders. The electrical properties of CMC spinel were correlated to the degree of crystallinity of the pelletized CMC spinel sintered at 1200 °C, but not influenced by their phase fraction. In addition, the electrical conductivity of CMC spinel is higher than that of the commonly used $Mn_{1.5}Co_{1.5}O_4$ spinel (60 Scm^{-1}) [12].

Figure 8. Arrhenius plot and temperature-dependent electrical conductivity (insert) of CMC spinel synthesized at different CA/MN ratios.

4. Conclusions

Dual-phase nanocrystalline CMC spinel powders consisting of cubic CuMnCoO and tetragonal Mn_2CoO_4 were successfully synthesized by the sol–gel method at different CA/MN ratios. The compositional homogeneity and phase purity were significantly affected by the CA/MN ratios. A small percentage of $CuCo_2O_4$ impurity phase was observed in the powder synthesized at a low amount of CA, particularly at a CA/MN ratio of 0.5. The impurity phase formed primarily because of the incomplete chelation of metal cations, thereby indicating a strong relationship among phase formation, the degree of crystallization of CMC spinel powders, and the CA amount used upon synthesis. The CA/MN ratio has influenced not only the phase formation and crystallinity of CMC spinel powders but also the particle size distributions, which later influenced their microstructure and electrical properties. In this work, the CA/MN ratio of 1.0 yielded the finest CMC spinel with the least agglomerates, thereby producing the highest electrical conductivity of 116 Scm^{-1}. Considering that the SOFC interconnects work as a current collector in the system, the coating material with high electrical conductivity is preferred. Therefore, the CA/MN ratio of 1.0 is recommended for the synthesis of homogenous CMC spinel powders.

Author Contributions: Conceptualization, A.M. and M.R.S.; methodology, J.C.W.M.; formal analysis, J.C.W.M.; investigation, I.A.; resources, M.R.S. and J.R.; writing—original draft preparation, J.C.W.M.; writing—review and editing, A.M.; visualization, I.A.; supervision, A.M.; funding acquisition, A.M. All authors have read and agreed to the published version of the manuscript.

Data Availability Statement: The data presented in this study are available on request from the corresponding author.

Acknowledgments: The authors would like to extend their gratitude to the Centre for Research and Instrumentation Management, Universiti Kebangsaan Malaysia for the use of their excellent testing equipment.

Conflicts of Interest: The authors declare no conflict of interest.

References

1. Mahmud, L.S.; Muchtar, A.; Somalu, M.R. Challenges in Fabricating Planar Solid Oxide Fuel Cells: A Review. *Sustain. Energy Rev.* **2017**, *72*, 105–116. [CrossRef]
2. da Silva, F.S.; de Souza, T.M. Novel Materials for Solid Oxide Fuel Cell Technologies: A Literature Review. *Int. J. Hydrog. Energy* **2017**, *42*, 26020–26036. [CrossRef]
3. Jiang, S.; Chen, X. Chromium Deposition and Poisoning of Cathodes of Solid Oxide Fuel Cells—A Review. *Int. J. Hydrog. Energy* **2014**, *39*, 505–531. [CrossRef]
4. Falk-Windisch, H.; Svensson, J.E.; Froitzheim, J. The Effect of Temperature on Chromium Vaporization and Oxide Scale Growth on Interconnect Steels for Solid Oxide Fuel Cells. *J. Power Source* **2015**, *287*, 25–35. [CrossRef]
5. Zhou, L.; Mason, J.H.; Li, W.; Liu, X. Comprehensive Review of Chromium Deposition and Poisoning of Solid Oxide Fuel Cells (SOFCs) Cathode Materials. *Renew. Sustain. Energy Rev.* **2020**, *134*, 110320. [CrossRef]
6. Mah, J.C.W.; Muchtar, A.; Somalu, M.R.; Ghazali, M.J. Metallic Interconnects for Solid Oxide Fuel Cell: A Review on Protective Coating and Deposition Techniques. *Int. J. Hydrog. Energy* **2017**, *42*, 9219–9229. [CrossRef]
7. Ni, H.; Gao, Z.; Li, X.; Xiao, Y.; Wang, Y.; Zhang, Y. Synthesis and Characterization of $CuFeMnO_4$ Prepared by Co-Precipitation Method. *J. Mater. Sci.* **2018**, *53*, 3581–3589. [CrossRef]
8. Zhang, X.; You, P.F.; Zhang, H.L.; Yang, X.G.; Luo, M.Q.; Zeng, C. Preparation and Performances of Cu–Co Spinel Coating on Ferritic Stainless Steel for Solid Oxide Fuel Cell Interconnect. *Int. J. Hydrog. Energy* **2018**, *43*, 3273–3279. [CrossRef]
9. Sreedhar, I.; Agarwal, B.; Goyal, P.; Singh, S.A. Recent Advances in Material and Performance Aspects of Solid Oxide Fuel Cells. *J. Electroanal. Chem.* **2019**, *848*, 113315. [CrossRef]
10. Masi, A.; Bellusci, M.; McPhail, S.J.; Padella, F.; Reale, P.; Hong, J.E.; Steinberger-Wilckens, R.; Carlini, M. Cu-Mn-Co Oxides as Protective Materials in SOFC Technology: The Effect of Chemical Composition on Mechanochemical Synthesis, Sintering Behaviour, Thermal Expansion and Electrical Conductivity. *J. Eur. Ceram. Soc.* **2016**, *37*, 661–669. [CrossRef]
11. Talic, B.; Falk-Windisch, H.; Venkatachalam, V.; Hendriksen, P.V.; Wiik, K.; Lein, H.L. Effect of Coating Density on Oxidation Resistance and Cr Vaporization from Solid Oxide Fuel Cell Interconnects. *J. Power Source* **2017**, *354*, 57–67. [CrossRef]
12. Zhao, Q.; Geng, S.; Chen, G.; Wang, F. Effect of NiFe2 Coating Thickness on High Temperature Oxidation and Electrical Behavior of Coated Steel Interconnect. *J. Alloys Compd.* **2021**, *858*, 157746. [CrossRef]
13. Rufner, J.F.; Castro, R.H.R.; Holland, T.B.; Benthem, K. Van Mechanical Properties of Individual $MgAl_2O_4$ Agglomerates and Their Effects on Densification. *Acta Mater.* **2014**, *69*, 187–195. [CrossRef]
14. Molin, S. Evaluation of Electrodeposited Mn-Co Protective Coatings on Crofer 22 APU Steel. *Int. J. Appl. Ceram. Technol.* **2018**, *15*, 349–360. [CrossRef]
15. Yang, H.; Zhu, M.; Li, Y. Sol–Gel Research in China: A Brief History and Recent Research Trends in Synthesis of Sol–Gel Derived Materials and Their Applications. *J. Sol-Gel Sci. Technol.* **2022**, 1–16, In press. [CrossRef]
16. Pang, W.K.; Lee, J.Y.; Wei, Y.S.; Wu, S.H. Preparation and Characterization of Cr-Doped LiMnO2 Cathode Materials by Pechini's Method for Lithium Ion Batteries. *Mater. Chem. Phys.* **2013**, *139*, 241–246. [CrossRef]
17. Samat, A.A.; Somalu, M.R.; Muchtar, A.; Hassan, O.H.; Osman, N. LSC Cathode Prepared by Polymeric Complexation Method for Proton-Conducting SOFC Application. *J. Sol-Gel Sci. Technol.* **2016**, *78*, 1–12. [CrossRef]
18. Danks, A.E.; Hall, S.R.; Schnepp, Z. The Evolution of 'Sol–Gel' Chemistry as a Technique for Materials Synthesis. *Mater. Horiz.* **2016**, *3*, 91–112. [CrossRef]
19. Bhagwat, V.R.; Humbe, A.V.; More, S.D.; Jadhav, K.M. Sol-Gel Auto Combustion Synthesis and Characterizations of Cobalt Ferrite Nanoparticles: Different Fuels Approach. *Mater. Sci. Eng. B Solid-State Mater. Adv. Technol.* **2019**, *248*, 114388. [CrossRef]
20. Wattanasiriwech, D.; Wattanasiriwech, S. Effects of Fuel Contents and Surface Modification on the Sol-Gel Combustion Ce0.9 Gd0.1O1.95 Nanopowder. *Energy Procedia* **2013**, *34*, 524–533. [CrossRef]
21. Sihaib, Z.; Puleo, F.; Pantaleo, G.; La Parola, V.; Valverde, J.L.; Gil, S.; Liotta, L.F.; Fendler, A.G. The Effect of Citric Acid Concentration on the Properties of LaMnO3 as a Catalyst for Hydrocarbon Oxidation. *Catalysts* **2019**, *9*, 226. [CrossRef]
22. Sadabadi, H.; Allahkaram, S.R.; Kordijazi, A.; Akbarzadeh, O.; Rohatgi, P.K. Structural Characterization of LaCoO3 Perovskite Nanoparticles Synthesized by Sol–Gel Autocombustion Method. *Eng. Rep.* **2021**, *3*, 1–7. [CrossRef]
23. Ranjeh, M.; Amiri, O.; Salavati-Niasari, M.; Shabani-Nooshabadi, M. Preparation and Study of Characteristics of $LiCoO_2/Fe_3O_4/Li_2B_2O_4$ nanocomposites as Ideal Active Materials for Electrochemical Hydrogen Storage. *RSC Adv.* **2021**, *11*, 23430–23436. [CrossRef]
24. Sijo, A.K. Influence of Fuel-Nitrate Ratio on the Structural and Magnetic Properties of Fe and Cr Based Spinels Prepared by Solution Self Combustion Method. *J. Magn. Magn. Mater.* **2017**, *441*, 672–677. [CrossRef]

25. Romero, M.; Faccio, R.; Martínez, J.; Pardo, H.; Montenegro, B.; Plá Cid, C.C.; Pasa, A.A.; Mombrú, Á.W. Effect of Lanthanide on the Microstructure and Structure of $LnMn_{0.5}Fe_{0.5}O_3$ Nanoparticles with Ln=La, Pr, Nd, Sm and Gd Prepared by the Polymer Precursor Method. *J. Solid State Chem.* **2015**, *221*, 325–333. [CrossRef]

26. Gouveia, D.S.; Rosenhaim, R.; Lima, S.J.G.; Longo, E.; De Souza, A.G.; Dos Santos, I.M.G. The Characterization of $Co_xZn_{7-X}Sb_2O_{12}$ Spinel Obtained by the Pechini Method. *Mater. Res.* **2005**, *8*, 213–219. [CrossRef]

27. Mah, J.C.W.; Muchtar, A.; Somalu, M.R.; Ghazali, M.J.; Raharjo, J. Formation of Sol–Gel Derived $(Cu,Mn,Co)_3O_4$ Spinel and Its Electrical Properties. *Ceram. Int.* **2017**, *43*, 7641–7646. [CrossRef]

28. Yang, X.Y.; Peng, X.; Chen, J.; Wang, F. hui Effect of a Small Increase in the Ni Content on the Properties of a Laser Surface Clad Fe-Based Alloy. *Appl. Surf. Sci.* **2007**, *253*, 4420–4426. [CrossRef]

29. Baharuddin, N.A.; Muchtar, A.; Somalu, M.R.; Kalib, N.S.; Raduwan, N.F. Synthesis and Characterization of Cobalt-Free SrFe0·8Ti0·2O3-δ Cathode Powders Synthesized through Combustion Method for Solid Oxide Fuel Cells. *Int. J. Hydrog. Energy* **2018**, *44*, 30682–30691. [CrossRef]

30. Ding, C.; Yin, W.; Cao, L.; Zeng, Y. Synthesis of Manganese-Zinc Ferrite Nanopowders Prepared by a Microwave-Assisted Auto-Combustion Method: Influence of Sol-Gel Chemistry on Microstructure. *Mater. Sci. Semicond. Process.* **2014**, *23*, 50–57. [CrossRef]

31. Brylewski, T.; Kucza, W.; Adamczyk, A.; Kruk, A.; Stygar, M.; Bobruk, M.; Dąbrowa, J. Microstructure and Electrical Properties of $Mn_{1+x}Co_{2-x}O_4$ ($0{\leq}x{\leq}1.5$) Spinels Synthesized Using EDTA-Gel Processes. *Ceram. Int.* **2014**, *40*, 13873–13882. [CrossRef]

32. Kobler, A.; Lohmiller, J.; Schäfer, J.; Kerber, M.; Castrup, A.; Kashiwar, A.; Gruber, P.A.; Albe, K.; Hahn, H.; Kübel, C. Deformation-Induced Grain Growth and Twinning in Nanocrystalline Palladium Thin Films. *Beilstein J. Nanotechnol.* **2013**, *4*, 554–566. [CrossRef] [PubMed]

33. Dell'Agli, G.; Mascolo, G.; Mascolo, M.C.; Pagliuca, C. Weakly-Agglomerated Nanocrystalline $(ZrO_2)0.9(Yb_2O_3)$ 0.1 Powders Hydrothermally Synthesized at Low Temperature. *Solid State Sci.* **2006**, *8*, 1046–1050. [CrossRef]

34. Spiridigliozzi, L.; Dell'agli, G.; Biesuz, M.; Sglavo, V.M.; Pansini, M. Effect of the Precipitating Agent on the Synthesis and Sintering Behavior of 20 Mol% Sm-Doped Ceria. *Adv. Mater. Sci. Eng.* **2016**, *2016*, 1–8. [CrossRef]

35. Sharma, A.D.; Mukhopadhyay, J.; Basu, R.N. Synthesis and Characterization of Nanocrystalline MnCo2O4-d Spinel for Protective Coating Application in SOFC. *ECS Trans.* **2011**, *35*, 2509–2517. [CrossRef]

36. Schmidt, R.; Basu, A.; Brinkman, A.W. Small Polaron Hopping in Spinel Manganates. *Phys. Rev. B Condens. Matter Mater. Phys.* **2005**, *72*, 12–14. [CrossRef]

37. Majedi, A.; Abbasi, A.; Davar, F. Green Synthesis of Zirconia Nanoparticles Using the Modified Pechini Method and Characterization of Its Optical and Electrical Properties. *J. Sol-Gel Sci. Technol.* **2016**, *77*, 542–552. [CrossRef]